JOURNAL OF SPACECRAFT AND ROCKETS
Vol. 40, No. 3, May–June 2003

Chimera Simulations of Supersonic Flows over a Complex Satellite Launcher Configuration

Edson Basso*
Instituto Tecnológico de Aeronáutica, 12228-900 São José dos Campos, São Paulo, Brazil
Alexandre P. Antunes†
Embraer S.A., 12227-901 São José dos Campos, São Paulo, Brazil
and
João Luiz F. Azevedo‡
Instituto de Aeronáutica e Espaço, 12228-904 São José dos Campos, São Paulo, Brazil

An effort is underway to develop a chimera flow simulation code capable of handling the external aerodynamics of general launch vehicle configurations. Aerodynamic results are presented referring to inviscid, laminar, and turbulent viscous simulations of the first Brazilian satellite launch vehicle during its first-stage flight. The finite difference method is applied to the governing equations, written in conservation-law form for general body conforming curvilinear coordinates. The spatial discretization is accomplished with a central difference scheme in which artificial dissipation terms, based on a scalar, nonisotropic model, are added to the numerical scheme to maintain stability. The time-marching process is accomplished with a five-stage, second-order accurate, Runge–Kutta scheme. Studies of mesh refinement are also presented as a part of the validation effort, with the objective of providing a certified flow simulation capability for actual engineering work.

Nomenclature

a	=	speed of sound
C_p	=	pressure coefficient
$\bar{E}$, $\bar{F}$, and $\bar{G}$	=	inviscid flux vectors
$\bar{E}_v$, $\bar{F}_v$, and $\bar{G}_v$	=	viscous flux vectors
e	=	total energy per unit volume
J	=	Jacobian of the transformation
M	=	Mach number
p	=	pressure
$\bar{Q}$	=	vector of conserved variables
Re	=	Reynolds number
U, V, and W	=	contravariant velocity components
u, v, and w	=	Cartesian velocity components
α	=	angle of attack
γ	=	ratio of specific heats
δ	=	standard three-point central difference operators
$\bar{\delta}$	=	midpoint central difference operators
ρ	=	density

Subscript

∞	=	freestream quantities

Introduction

IN the present work, both inviscid and laminar and turbulent viscous simulations are performed, with the objective of reproducing the aerodynamic and thermodynamic phenomena that are present during the first-stage flight of the first Brazilian satellite launch vehicle (VLS). This work is part of an effort to develop the computational tools necessary to simulate aerodynamic flows over aerospace geometries, especially those related to the VLS system. A historical perspective of the development of computational fluid dynamics tools for flow simulation over general launch vehicle configurations at the institutions represented here can be found in Ref. 1.

The VLS presents a quite complex geometric configuration that has four strap-on boosters around a central core. An outline of this configuration is presented in Fig. 1. The four lateral boosters are arranged symmetrically around the central body, and they are the vehicle first stage. Therefore, mesh generation for flow simulation during the first-stage flight can be a very laborious process, with either structured or unstructured grid technologies. Actually, both approaches for the mesh generation are being pursued in the research group, but the results that will be presented in this work are solely concerned with the use of structured grids.

The initial attempts to generate a good structured grid over the complete VLS configuration resorted to a patched multiblock approach. However, the quality of the meshes so generated was not adequate for the flow simulations intended. Therefore, the use of patched meshes was discarded. Because the research group had a fair amount of experience in the use of structured grids for launch vehicle simulations,[2,3] the next natural option was to use overset, or chimera, grids. The initial objective of the use of overset multiblock meshes can enable the generation of better quality grids for the problems at hand. The code for the simulation of the flow over the VLS with this overset multiblock approach was obtained as a continuation of the development of the code already available for single-block flow simulations.[4] The single block code is based on the three-dimensional Euler formulation, and it has already been validated using data for the VLS and other sounding rockets presently being considered at Instituto de Aeronáutica e Espaço (IAE).[4]

The governing equations are assumed to be written in conservative form, and these equations are discretized by a finite difference method. Spatial discretization uses second-order accurate, central difference operators. The time-marching method is based on a five-stage, Runge–Kutta algorithm[5] that also has second-order accuracy in time. The artificial dissipation terms added are based on the nonisotropic, Turkel and Vatsa model.[6] Some initial three-dimensional

Received 13 July 2001; revision received 15 December 2002; accepted for publication 10 January 2003.

*Ph.D. Student, Department of Aeronautical Engineering; currently Research Engineer, Space Systems Division, Instituto de Aeronáutica e Espaço, Centro Técnico Aeroespacial, 12228-904 São José dos Campos, São Paulo, Brazil; basso@iae.cta.br.

†Project Engineer, Computational Aerodynamics Branch; alexandre.antunes@embraer.com.br.

‡Head, Aerodynamics Subdivision, Space Systems Division, Instituto de Aeronáutica et Espaço, Centro Técnico Aeroespacial; azevedo@iae.cta.br. Senior Member AIAA.

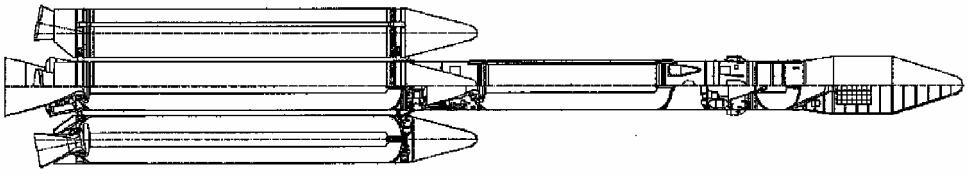

Fig. 1 Schematic of the VLS system during its first-stage flight.

results have been presented in Ref. 7, although using a somewhat different time-marching scheme. This reference treats simpler geometries, but it validates several of the concepts that are used as building blocks in the present effort. In the present case, the overset multiblock grid technique, or chimera technique,[8,9] is used to simulate flows over the complete VLS vehicle. This technique provides the capability to use structured meshes for the discretization of the calculation domain over truly complex configurations. Moreover, the chimera technique also allows for grid refinement characteristics that are similar to those achieved with unstructured meshes.

The forthcoming sections will present the governing equations, together with some details of the numerical method used for their solution. A brief discussion of the boundary conditions implemented is also presented, as well as an overview of the chimera grid procedure used in the present code. Inviscid, viscous laminar and turbulent solutions for the complete VLS vehicle are presented and discussed. The viscous calculations are performed through the solution of the Reynolds-averaged Navier–Stokes equations, whereas the inviscid cases are solved using the Euler equations. Note that the code implemented is intended to be used in a routine basis at IAE for aerodynamic analysis of the aerospace configurations of interest at the institute. The paper concludes with a critical evaluation of the flow simulation capability implemented and a discussion of perspectives for future work.

Governing Equations

It is assumed that the flows of interest in the present work can be represented by the Navier–Stokes equations in three dimensions. These equations can be written in conservation-law form for a curvilinear coordinate system as

$$\frac{\partial \bar{\boldsymbol{Q}}}{\partial \tau} + \frac{\partial}{\partial \xi}(\bar{\boldsymbol{E}} - \bar{\boldsymbol{E}}_v) + \frac{\partial}{\partial \eta}(\bar{\boldsymbol{F}} - \bar{\boldsymbol{F}}_v) + \frac{\partial}{\partial \varsigma}(\bar{\boldsymbol{G}} - \bar{\boldsymbol{G}}_v) = 0 \tag{1}$$

where $\bar{\boldsymbol{Q}}$ is the vector of conserved variables, defined as

$$\bar{\boldsymbol{Q}} = J^{-1}[\rho, \rho u, \rho v, \rho w, e]^T \tag{2}$$

The T superscript indicates the matrix transpose operation. For the inviscid calculations, $\bar{\boldsymbol{E}}_v$, $\bar{\boldsymbol{F}}_v$, and $\bar{\boldsymbol{G}}_v$ are assumed equal to zero. The $\bar{\boldsymbol{E}}$ and $\bar{\boldsymbol{E}}_v$ vectors can be written as

$$\bar{\boldsymbol{E}} = \begin{Bmatrix} \rho U \\ \rho u U + \xi_x p \\ \rho v U - \xi_y p \\ \rho w U - \xi_z p \\ (e + p)U - \xi_t p \end{Bmatrix} \tag{3}$$

$$\bar{\boldsymbol{E}}_v = J^{-1} Re^{-1} \begin{Bmatrix} 0 \\ \xi_x \tau_{xx} + \xi_y \tau_{xy} + \xi_z \tau_{xz} \\ \xi_x \tau_{yx} + \xi_y \tau_{yy} + \xi_z \tau_{yz} \\ \xi_x \tau_{zx} + \xi_y \tau_{zy} + \xi_z \tau_{zz} \\ \xi_x \beta_x + \xi_y \beta_y + \xi_z \beta_z \end{Bmatrix} \tag{4}$$

with similar expressions for the other flux vectors. The complete expressions for the inviscid flux vectors can be found in Ref. 10, and expressions for the viscous flux vectors, as implemented here, can be found, for instance, in Ref. 11. Note that, consistent with earlier comments, the cross-derivative terms were eliminated in the definition of the viscous flux vectors actually implemented in the code. Expressions for the Jacobian of the transformation, J, as well as for the various metric terms, can be found in Refs. 10 and 12, among other references. The pressure can be obtained from the equation of state for a perfect gas as

$$p = (\gamma - 1)\left[e - \tfrac{1}{2}\rho(u^2 + v^2 + w^2)\right] \tag{5}$$

A suitable nondimensionalization of the governing equations has been assumed in writing Eq. (1). In particular, the values of flow properties are made dimensionless with respect to freestream quantities, as described in Ref. 12.

The governing equations are discretized in a finite difference context on structured hexahedral meshes, which would conform to the bodies in the computational domain. Because a central difference spatial discretization method is being used, artificial dissipation terms must be added to the formulation to control nonlinear instabilities for both inviscid and viscous cases. The artificial dissipation terms used here are based on Turkel and Vatsa's scalar model.[6] This model is nonlinear and nonisotropic, with the scaling of the artificial dissipation operator in each coordinate direction weighted by its own spectral radius of the corresponding flux Jacobian matrix. The residue operator is defined as the evaluation of the discretized partial differential equation (or system of partial differential equations), and, in this way, the numerical value of the residue operator represents how well the evaluation of the discretized form of the equations is satisfied by the current solution in the present iteration level n. The artificial dissipation terms are added to the residue operator to maintain nonlinear stability. In the present implementation, the residue operator (RHS) is defined as

$$\mathrm{RHS}^{(l)}_{i,j,k} = \Delta t_{i,j,k}\left\{\delta_\xi(\bar{\boldsymbol{E}})_{i,j,k} - \bar{\delta}_\xi\left[\left(\bar{\boldsymbol{E}}_v + J^{-1}d\right)_{i,j,k}\right] + \delta_\eta(\bar{\boldsymbol{F}})_{i,j,k}\right.$$

$$\left. - \bar{\delta}_\eta\left(\bar{\boldsymbol{F}}_v + J^{-1}d\right)_{i,j,k} + \delta_\varsigma(\bar{\boldsymbol{G}})_{i,j,k} - \bar{\delta}_\varsigma\left(\bar{\boldsymbol{G}}_v + J^{-1}d\right)_{i,j,k}\right\} \tag{6}$$

The δ_ξ, δ_η, and δ_ς terms represent standard three-point central difference operators in the ξ, η, and ς directions, respectively. Similarly, $\bar{\delta}_\xi$, $\bar{\delta}_\eta$, and $\bar{\delta}_\varsigma$ are the midpoint central difference operators. The artificial dissipations operators, $d_{i\pm 1/2,j,k}$, $d_{i,j\pm 1/2,k}$, and $d_{i,j,k\pm 1/2}$, which would appear from the application of the difference operators indicated in Eq. (6), are defined precisely in Ref. 6.

Because steady-state solutions are the major interest of the present study, a variable time-step convergence acceleration procedure has been implemented. In the present case, the time step is defined as follows, wherein the Courant–Friedrichs–Lewy (CFL) number is included:

$$\Delta t_{i,j,k} = \mathrm{CFL}/c_{i,j,k} \tag{7}$$

The characteristic velocity, $c_{i,j,k}$, is defined as

$$c_{i,j,k} = \max\left(|U| + a\sqrt{\xi_x^2 + \xi_y^2 + \xi_z^2}\right.$$

$$\left.|V| + a\sqrt{\eta_x^2 + \eta_y^2 + \eta_z^2}, \qquad |W| + a\sqrt{\varsigma_x^2 + \varsigma_y^2 + \varsigma_z^2}\right)_{i,j,k} \tag{8}$$

where U, V, and W are the contravariant velocity components in the ξ, η, and ς directions, respectively.

The time marching is performed based on a five-stage, second-order accurate, hybrid Runge–Kutta time-stepping scheme:

$$Q_i^{(0)} = Q_i^n, \qquad Q_i^{(l)} = Q_i^{(0)} - \alpha_l\,\mathrm{RHS}^{(l-1)}, \qquad l = 1, \ldots, 5$$

$$Q_i^{n+1} = Q_i^{(5)} \tag{9}$$

Here, the α_l constants are defined as $\alpha_1 = \frac{1}{4}$, $\alpha_2 = \frac{1}{6}$, $\alpha_3 = \frac{3}{8}$, $\alpha_4 = \frac{1}{2}$, and $\alpha_5 = 1$. Note that only the convective operator inside the RHS term indicated in Eq. (4) is actually evaluated at every time step. The viscous flux vectors are only evaluated at the first stage of the Runge–Kutta time-stepping scheme. Moreover, the artificial dissipation terms are evaluated at alternate stages (i.e., at the odd stages in the present case of the time-marching procedure) for the viscous calculations. In the inviscid case, artificial dissipation terms are evaluated only in the two initial stages of the Runge–Kutta time-stepping method. It can be shown that this provides enough damping to maintain nonlinear stability,[5,13] whereas it yields a more efficient numerical scheme.

Finally, turbulent simulations have used the Baldwin and Lomax[14] algebraic eddy viscosity model to provide turbulence closure. The turbulence model was implemented in this work in its standard form as described by Baldwin and Lomax.[14] Because this model is very well known and its expressions are widely available, they will not be included here.

Boundary Conditions

For the inviscid calculations, the boundary conditions for the rocket surface are based on that there should be no flow through a solid surface. The no-flow condition is imposed in the present context by forcing the contravariant velocity component normal to the wall, V, to be identically zero in the flux calculations. Aside from this boundary condition enforcement at the flux calculation stage, conserved properties at the wall points are simply obtained by zeroth-order extrapolation of their nearest neighbor in the nominally wall-normal direction. Although extremely simple, this boundary condition enforcement procedure has proved to be quite adequate with the present algorithm. The velocity boundary conditions for the rocket surface for the viscous calculations are based on the no-slip condition for a solid surface. Furthermore, the wall is assumed to be adiabatic, and a zero normal pressure gradient is assumed, to obtain all conserved properties at the wall.

Freestream conditions are imposed at the upstream and lateral far-field boundaries for both inviscid and viscous cases. The upstream centerline is a singularity of the coordinate transformation. Hence, properties at this computational boundary are obtained by zeroth-order extrapolation from the corresponding points in the longitudinal direction, followed by the averaging of these extrapolated values in the azimuthal direction. Note that all azimuthal planes converge to a single physical point along the upstream centerline. Hence, averaging values in the azimuthal direction is a necessary step to guarantee that all points in computational space that correspond to a single point in physical space have the same values for the conserved properties.

All quantities are obtained by extrapolation of interior data at the downstream boundaries for the inviscid cases. For the viscous cases, the same boundary condition is applied for the downstream boundaries, although this would not be strictly correct in this case due to the existence of a boundary layer. Note that, because there is subsonic flow inside the boundary layer, information can actually propagate upstream, even if the flow outside the boundary layer is supersonic. Nevertheless, arguments of implementation simplicity led to the use of such straightforward downstream boundary condition implementation even for viscous flows. Also note that there has been no observed degradation in result quality due to this simplification. Furthermore, zeroth-order extrapolation is used in this case to further simplify the code implementation. The use of such a simplified boundary condition at the downstream boundary is possible because only supersonic flight conditions are addressed.

Because both simulations, including the complete vehicle and including only one-half vehicle, were performed, two types of boundary conditions had to be implemented in the azimuthal direction for the central body grid. Hence, if the complete vehicle is included, periodic conditions are used in the azimuthal direction. For the cases in which a symmetry plane is assumed, symmetry boundary conditions are used for the central body mesh. In this case, two additional computational planes are included across the pitching plane to enforce the symmetry conditions. For the booster grids, periodic boundary conditions are always adopted in the azimuthal direction for all cases considered here. Interior boundaries, which are created by the multiblock approach, are handled by the chimera property interpolation procedure that is described in the next section.

Chimera Technique

The mesh point distribution over the physical domain in which the flow is to be computed is always a critical aspect for a successful calculation. Grid point distribution must be balanced enough to cover the entire flowfield, avoiding regions with excessive grid coarseness. On the other hand, points must be clustered in regions in which phenomena, such as expansions and shock waves, occur without exceeding the available computational resources. The computational meshes used in the present work are all generated by the multisurface algebraic technique.[15] Note that, although the complete VLS configuration is fairly complex, each body that comprises this geometry is actually very simple. Therefore, each individual mesh can be generated in a two-dimensional, axisymmetric fashion and then rotated in the azimuthal direction to create the actual three-dimensional grid. For the VLS configuration, five component meshes are generated, one for each body that comprises the complete configuration. Figure 2 exhibits one longitudinal plane of the volume mesh and the surface grid for the VLS central body. Note that, although the present work has both Euler and Navier–Stokes solutions, some of the meshes used in the inviscid calculation have a fair amount of grid stretching toward the wall. This grid stretching is the result of an attempt to capture details of the shock reflection phenomena that are expected to occur in the cluster region. Another important aspect is the need for a sufficient number of points between the lateral boosters and the central rocket body for an adequate behavior of the chimera hole-cutting process. In this process, points of both meshes are eliminated from the set of active points in the domain either for being outside the flow region of interest or to avoid an excessively large region of overlap. The hole-cutting process is performed with sufficient care to allow the formation of an interpolation region among the points of adjacent meshes. The existence of a larger number of points in those overlapping areas brings an improvement in the precision of the information exchange among the meshes at the expense of increasing the computational costs.

The present work uses trilinear interpolation to pass information at each mesh interior boundary point. Note that there is no attempt to satisfy conservation in this interpolation process. Because shocks may be crossing the interface between grid blocks, it would be interesting to have the enforcement of some conservation statement at grid interfaces. However, the conservative interface treatment is not included in the present case due to the high computational costs associated with such an implementation, especially in the three-dimensional case, and because the present effort should be seen as

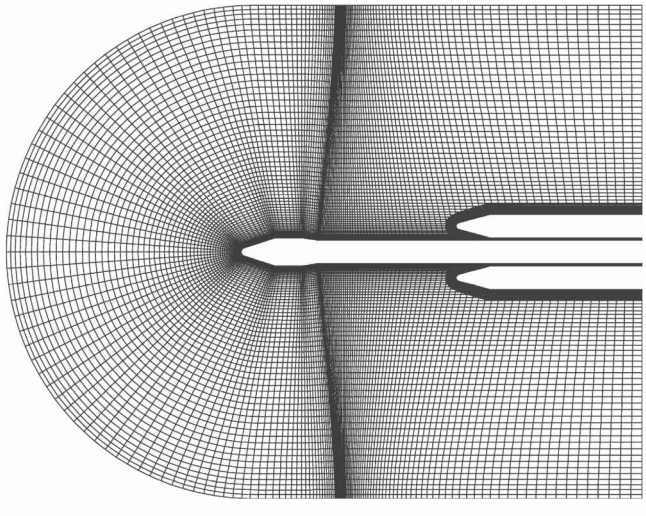

Fig. 2 Computational meshes for the complete VLS configuration after the hole-cutting process: a two-dimensional visualization.

an evolutionary step toward a more complete simulation capability. A conservative method at the interfaces among chimera meshes that satisfies the conservation laws was developed by Wang and Yang.[8] A detailed discussion of the approaches for handling these interior boundary conditions can be found in Ref. 9.

The code, which actually performs the hole-cutting process, is a tool developed in-house by the group. In the case of the VLS meshes, the code performs the logic elimination of the mesh points that are inside the other bodies and, therefore, out of the calculation domain. Notice that only the points that are inside the other bodies of the configuration and, therefore, out of the calculation domain, are removed. The solution process in the flow solver essentially considers the following main steps: 1) An initial condition is imposed for all meshes. 2) An order of operation throughout the various meshes is defined. 3) The residue is calculated in the first mesh. 4) The new solution is calculated for the first mesh interior points. 5) Boundary conditions are updated for this first mesh. 6) The points along the hole boundary are updated in all meshes, which have some overlapping with this first mesh. 7) The process is restarted from step 3 with the next mesh.

This process is repeated until all of the meshes have reached the new solution level at time $(n+1)\Delta t$. Afterward, convergence of the solution is verified. If the convergence criterion is not satisfied, the process is restarted from step 3. Furthermore, the chimera interior boundaries consider a double fringe point approach. Such an approach allows for the use of the same computational stencil for the artificial dissipation terms either at a block interior point or at a block boundary point. This approach also facilitates the implementation of the viscous terms in the present case.

Results and Discussion

The results presented here refer to simulations of the flow over the VLS vehicle during its first-stage flight. The specific results included consider only the case with freestream Mach number equal to 2 and zero angle of attack. These conditions are representative of the simulations performed so far for this configuration. Moreover, because the flight time in the lower atmosphere for these satellite launchers is very short, and the vehicle is at supersonic speeds during most of this flight, it seems appropriate to select a supersonic flight condition for the present discussion. Furthermore, the purpose of the present paper lies mostly in the description of the capability implemented instead of a detailed account of the VLS aerodynamics. Interesting aspects of the multiblock mesh technology can be analyzed for supersonic flight conditions. In particular, there is interest in evaluating the procedure adopted for communication of information across the internal boundaries among blocks with discontinuities in the flow properties. As mentioned earlier, the major interest in this work concerns the evaluation of the chimera technique usage as a tool for flow analysis on geometries of interest for the institutions represented here. Furthermore, the results described here should be seen as a continuation of the code validation effort. One should observe that the group has already performed some three-dimensional Chimera simulations, but these only considered fairly simple geometric configurations. In the present case, a truly realistically complex configuration is being considered that brings evidence of the possible uses of the capability for practical vehicle design activities.

Inviscid Simulations

The complete mesh system used in the inviscid simulations was divided into five component meshes. One of these discretizes the computational domain around the central body using $120 \times 65 \times 33$ grid points in the longitudinal, normal, and circumferential directions, or ξ, η, and ς directions, respectively. Four identical meshes are used for the boosters. Each of them has $120 \times 36 \times 33$ points in the longitudinal, normal, and circumferential directions, respectively. Note from Fig. 2 that the afterbody portion of the vehicle has been simplified for the simulations reported here. This simplification has been performed because previous experience with afterbody flows[16] has demonstrated the need for a viscous turbulent formulation for the adequate description of such flows. In the future,

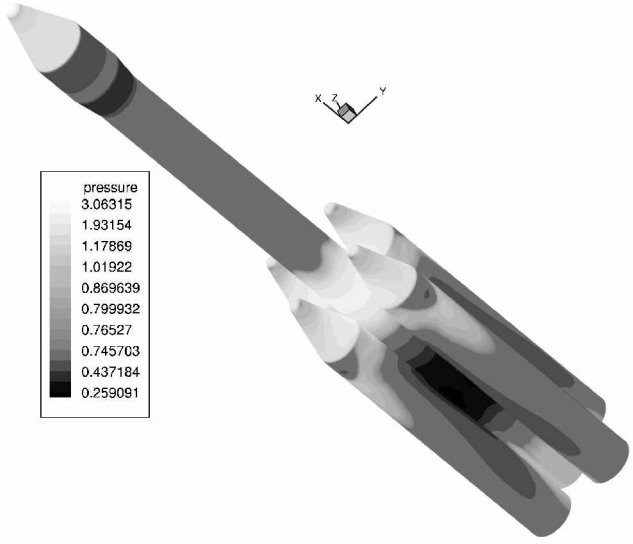

Fig. 3 Pressure contours on the surface of the vehicle for $M_\infty = 2$ and zero angle of attack.

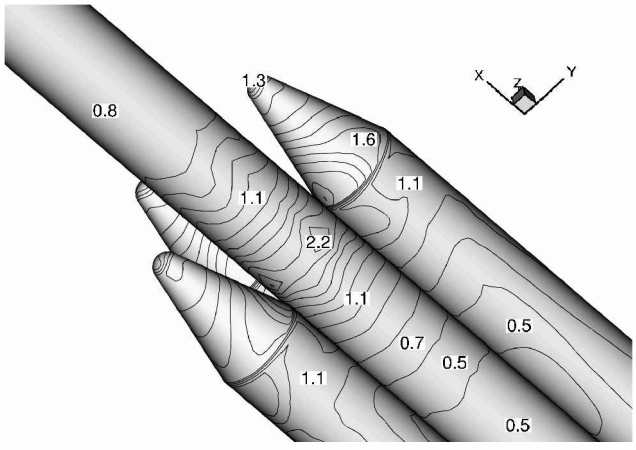

Fig. 4 Pressure contours on the surface of the vehicle around booster nosecaps for $M_\infty = 2$ and zero angle of attack.

a detailed representation of the afterbody will be included in the vehicle model, but flow simulation in the afterbody region is beyond the scope of the present effort. Furthermore, the added complexity in the afterbody region would not contribute to the major interest of the present work.

A view of the pressure contours along the vehicle can be seen in Fig. 3. The strong flow compressions in the rocket front areas, indicating the flow stagnation points and a quite noticeable pressure increase in the region on the central body immediately downstream of the boosters noses, can be seen clearly in Fig. 3. This region of high pressure is due the phenomenon of convergence of the booster bow shock. Therefore, downstream of this region, there is a pressure decrease, which can also be observed in Fig. 3. The flow, which crosses the booster detached bow shocks, has a tendency to move outward due to the high-pressure region just downstream of the booster noses. This outward motion of the flow is responsible for the low-pressure region downstream of the shock impingement point along the central body. Pressure levels in the region between the boosters and the central body can be very important during the first-stage separation process. An enlarged view of the region around the booster nose caps can be seen in Fig. 4, which again displays dimensionless pressure contours on the body surface. The meshes used to discretize the vehicle in this simulation do not offer sufficient resolution to visualize all of the flow phenomena in the interaction region and within the necessary accuracy limits. This lack of resolution can be observed in Fig. 4 in the rather smooth variation of

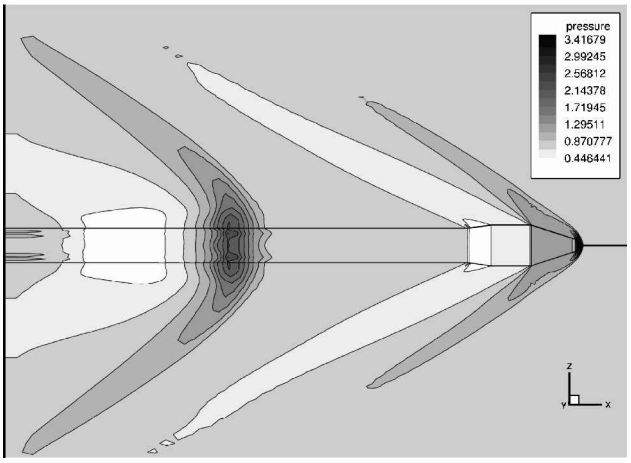

Fig. 5 Pressure contours for a longitudinal plane without boosters for the VLS at $M_\infty = 2$ and zero angle of attack.

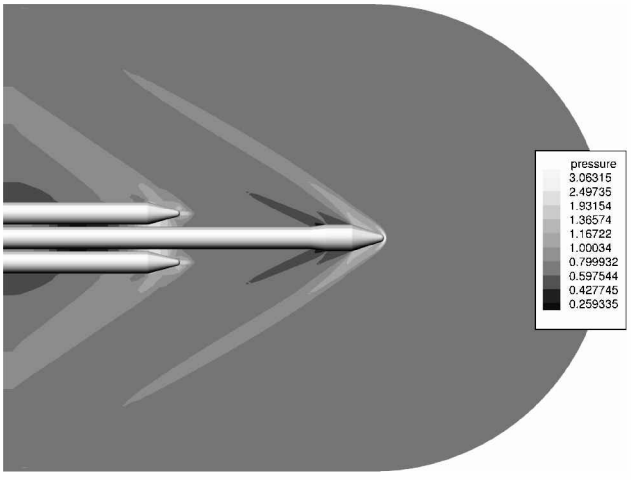

Fig. 6 Pressure contours on the central body and two opposing boosters for the VLS at $M_\infty = 2$ and zero angle of attack.

the dimensionless pressure contour lines in a region where shock waves should be present.

Figure 5 shows pressure contours for a longitudinal plane along the vehicle, which does not include any boosters. This longitudinal plane is formed by a cut in the complete mesh at an azimuthal position, which is a symmetry plane between two boosters. The imprint on this plane of the high- and low-pressure regions described earlier can also be seen clearly in Fig. 5. Figure 6 shows pressure contours for a longitudinal plane along the vehicle. This longitudinal plane is equivalent to the one shown in Fig. 2. In Fig. 6, a longitudinal plane that contains the central body and two boosters is selected. The plots in Figs. 5 and 6 clearly indicate the bow shock wave ahead of the vehicle, the expansion that occurs at the forebody cone–cylinder intersection, the expansion region along the boattail, and the compression region ahead of the boosters. Note that the formation of the detached shock ahead of the boosters is clearly captured by the method, whereas its reflections are not. This behavior can be attributed to a lack of resolution of the computational mesh used for the current simulation.

Mach numbers contours along the region between the central body and the boosters are shown Fig. 7. One can observe in the central body surface Mach number contours that there is an acceleration of the flow downstream of the low-speed region, discussed earlier, as a consequence of the expansion that occurs in the booster's cone–cylinder intersection. This is further accentuated by the deviation of the flow caused by the high-pressure region. Furthermore, the influence of the shock reflections over the Mach number contours distribution on the surface of the boosters can also be seen in Fig. 7.

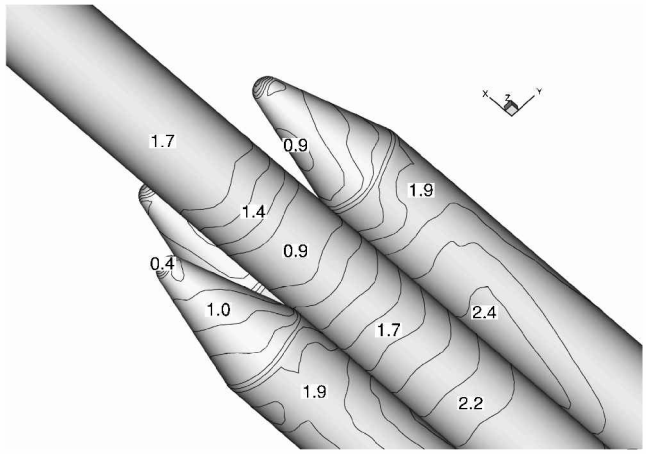

Fig. 7 Mach number contours on the surface of the vehicle for $M_\infty = 2$ and zero angle of attack.

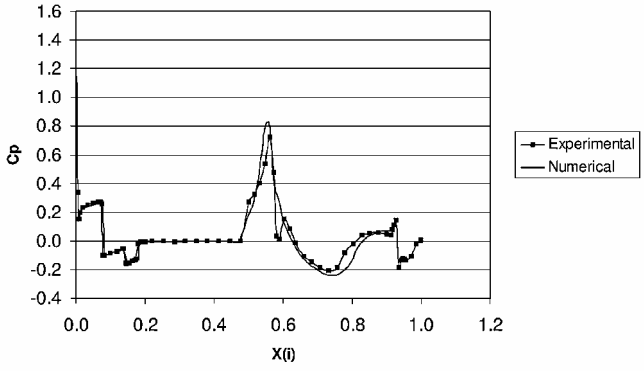

Fig. 8 Comparison of central body pressure coefficient distributions for a longitudinal plane including a booster ($M_\infty = 2$ and $\alpha = 0$ deg).

One of the reasons for the selection of the present test case is the existence of experimental data for this flight condition. These experimental data and details of the wind-tunnel tests are described in Ref. 17. Figure 8 exhibits a comparison of the C_p distributions along the vehicle's central body with the experimental data. In this case, a longitudinal plane that contains the central body and two booster axes is selected for the comparison. In other words, the comparison indicates the agreement of the data for a plane of the central body corresponding to the cut indicated in Fig. 6. One can observe that the agreement in the forebody portion of the vehicle is very good. The agreement in the afterbody region, especially where there is a close proximity between the central body and booster, is not as good. However, some aspects of the results in this downstream portion of the vehicle can be explained and/or deserve further comment.

First, note that the experimental data indicate that the reflection of the booster bow shock wave is at x/L approximately equal to 0.6. The computational results show some change in the C_p curve slope at this location, but they do not have the second pressure coefficient peak, which can be seen in the experimental data. Further simulations are currently being performed to try to understand the reasons for such a difference. On the other hand, the striking difference in the results downstream of $x/L = 0.92$ occurrs because the central body nozzle is not modeled in the present calculations, whereas it is present in the wind-tunnel model. There is also a fair amount of difference in the C_p distributions in the $0.75 < x/L < 0.90$ range. It is believed that a large percentage of the differences observed in this region can be attributed to viscous effects because the gap between the central body and boosters is very small in this region.

Because only flow conditions at low incidence are being considered in the present effort, one could take advantage of the flow symmetry to use a grid that imposes symmetry conditions along the pitch plane. This allows further grid refinement in all directions.

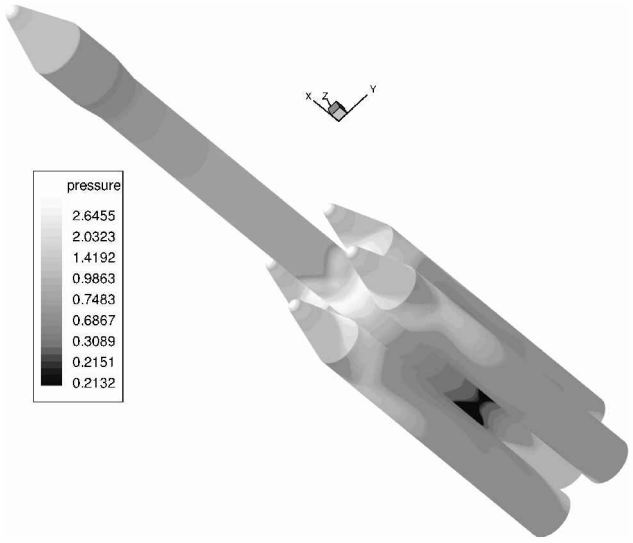

Fig. 9 Pressure contours on the surface of the vehicle ($M_\infty = 2$ and $\alpha = 0$ deg).

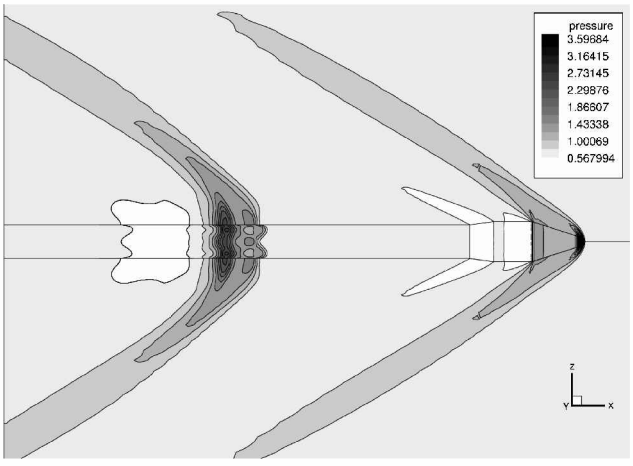

Fig. 10 Pressure contours for a longitudinal plane without boosters for the VLS booster ($M_\infty = 2$ and $\alpha = 0$ deg).

The forthcoming results considered, therefore, a composite grid with one-half of a central body and only two boosters. In this case, the central body mesh has $220 \times 50 \times 67$ grid points on the ξ, η, and ς curvilinear directions, respectively. The mesh for each booster has $220 \times 40 \times 33$ grid points in the same directions. Pressure contours for the surface of the vehicle are shown in Fig. 9 for this case. It is clear that the refinement has increased the accuracy of the results obtained. Shock smearing is considerably reduced with the finer mesh. Figure 10 shows pressure contours for a longitudinal plane along the vehicle, which does not include any boosters. The refinement effects can be seen in Fig. 11, where a detail of the region around the booster nose caps is presented. Figure 11 shows Mach number contours with a far superior resolution than those seen in Fig. 7, which represents the corresponding for the coarser grid.

The pressure coefficient distribution for the simulation with the finer grid is presented in Fig. 12. The agreement between experimental and computational results is certainly improved by the grid refinement. Also note in Fig. 12 that the pressure distribution in the upstream portions of the vehicle is essentially unaltered by the refinement. The differences start to appear at the booster bow shock impingement point on the central body surface. Furthermore, one can see that the position of the bow shock impingement point is in better agreement with the experimental data for the current fine mesh case. The high pressures caused by the booster bow shock are quickly attenuated due to the expansion region in the booster

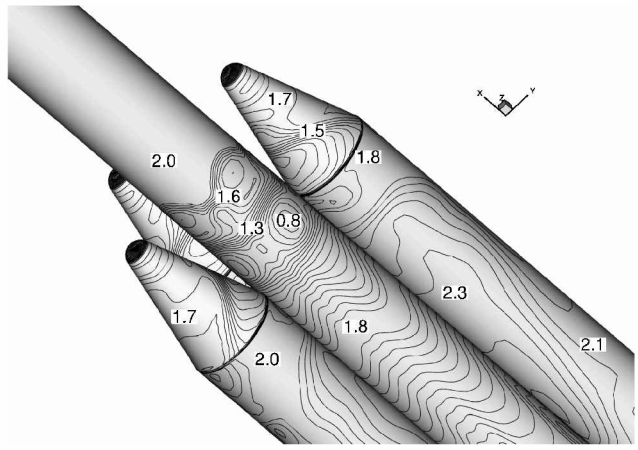

Fig. 11 Mach number contours on the surface of the vehicle booster ($M_\infty = 2$ and $\alpha = 0$ deg).

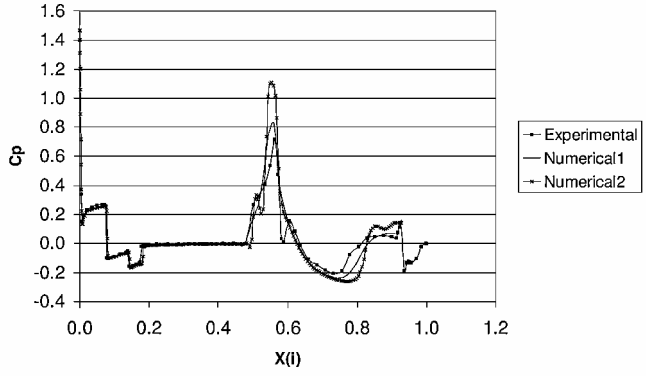

Fig. 12 Comparison of central body pressure coefficient distributions for a longitudinal plane including a booster ($M_\infty = 2$ and $\alpha = 0$ deg).

spherical-to-conical nose intersection. This effect cannot be seen in the experimental results, probably due to an insufficient quantity of pressure measurement points. The computational pressure coefficient value just after the shock presents an overshoot. Moreover, even with this finer grid, there is still no dramatic indication of the second peak in the C_p distribution that represents the second reflection of the booster detached shock on the central body surface.

Laminar Viscous Simulations

The meshes used for the first viscous simulations of the flow over the complete VLS had $120 \times 36 \times 33$ points in the ξ, η, and ς directions, respectively, for each of the booster grids and $120 \times 65 \times 33$ points for the central body. This grid is referred to here as the coarse grid. One should observe that this is same grid used for inviscid calculations, as already reported in Fig. 2. However, this grid has a refinement near the wall that is well beyond what would be required for an Euler solution. This approach was used on purpose to allow a comparison of inviscid and viscous calculations on the same grid. Furthermore, the actual complete configuration is used in the simulations, namely, the central body and four boosters are included in the definition of the computational domain. In these simulations, the freestream Mach number is assumed to be $M_\infty = 2.0$, and the angle of attack is zero. The Prandtl number is set to $Pr = 0.72$, and the Reynolds number is 1×10^7 based on the diameter of the central body of the vehicle. Figure 13 represents the Mach number contours in the longitudinal plane (plane 1) in Fig. 14.

The boundary-layer thickening along the central body surface, in the region immediately upstream of the lateral boosters, can be seen clearly in Fig. 13. The thickening of the boundary layer is initially a result of the detached bow shock's (ahead of the boosters) impingement on the central body surface. The information on the pressure rise due to shock impingement propagates upstream through the

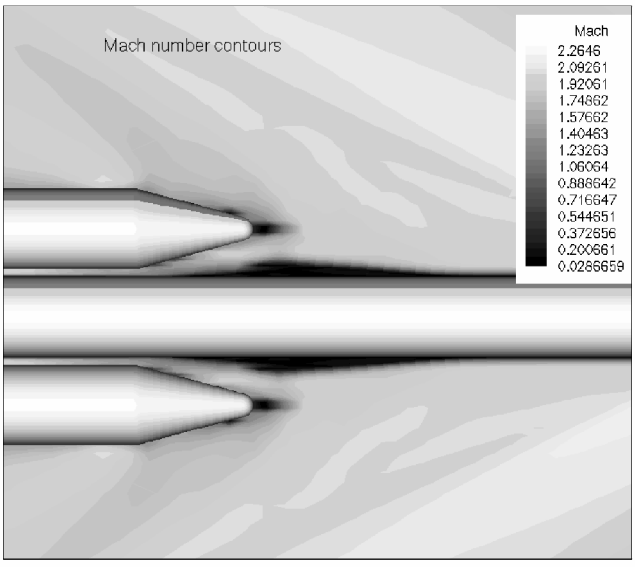

Fig. 13 Mach number contours on plane 1 (Fig. 14) for laminar flow simulations with the coarse grid ($M_\infty = 2$, $\alpha = 0$ deg, $Re = 1 \times 10^7$).

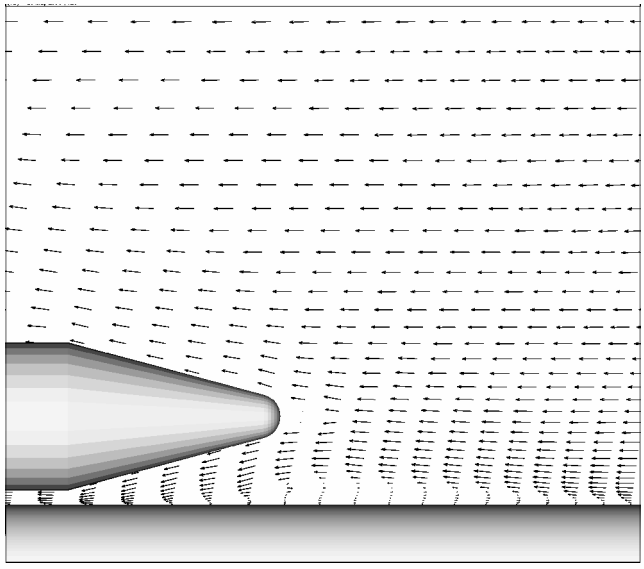

Fig. 15 Detail of the velocity vector plot around the booster nose cap for laminar simulations with the coarse grid ($M_\infty = 2$, $\alpha = 0$ deg, $Re = 1 \times 10^7$).

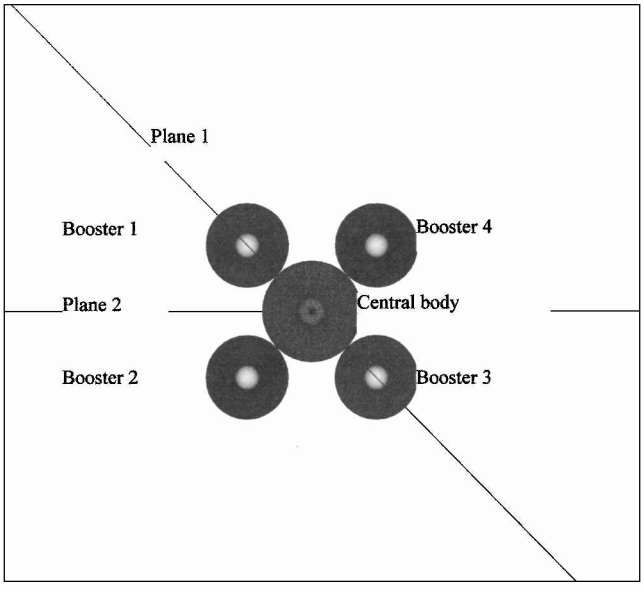

Fig. 14 Top view of complete VLS configuration indicating some of the planes in which vehicle results are presented.

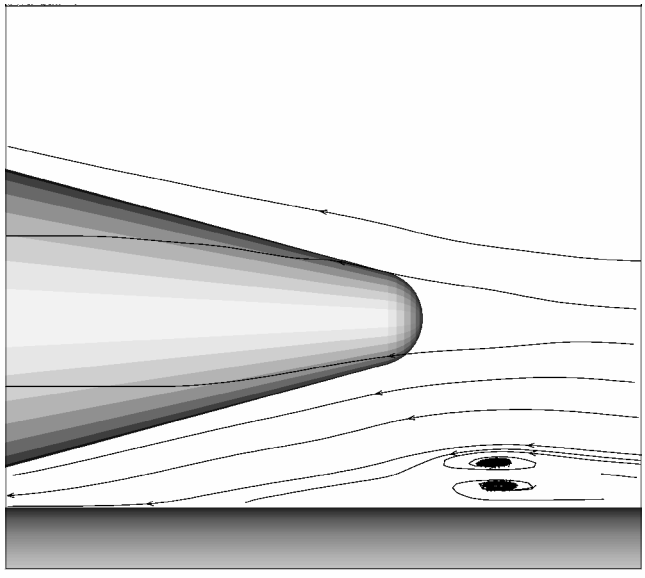

Fig. 16 Streamlines near the booster nose for coarse grid laminar simulations ($M_\infty = 2$, $\alpha = 0$ deg, $Re = 1 \times 10^7$).

boundary layer. Eventually, the information on the pressure rise due to shock impingement causes flow separation upstream of the impingement point due to the weakening of the boundary-layermomentum. Boundary-layer separation, on the other hand, causes the creation of an oblique shock wave, which, unfortunately, is not clearly seen in Fig. 13. This oblique shock wave is more readily seen on pressure contour plots. Note that these flow features ahead of the booster nose caps are not present in the Euler simulations. The overall flow topology indicates that, even with coarse grids, the viscous solutions are providing flow structures that are different from these seen in the Euler cases.

Figure 15 presents the velocity vectors in a flow plane that contains the central body axis and the axes of two boosters (plane 1 in Fig. 14). In particular, Fig. 15 shows the details of the flowfield just upstream of the booster forward aerodynamic fairing. Note that only velocity vectors corresponding to grid points in the central body mesh, in the cited plane, are represented in Fig. 15. Velocity vectors associated with points in the booster grid were suppressed from Fig. 15 to allow for a better visualization of the flowfield in the region. Flow deviation due to the booster is clearly seen in Fig. 15. Furthermore, one can also clearly see in Fig. 15 the recirculation region that extends from approximately 2.5 booster diameters upstream of the booster nose until well within the conical booster section. The velocity profiles along a portion of this separation region also seem to indicate that there is even a secondary separation within the recirculation region. The streamline plot shown in Fig. 16 corroborates this last observation. It must be emphasized, though, that Fig. 16 only shows a portion of the region depicted in Fig. 15, and, hence, it does not include the complete separation region.

Pressure coefficient distributions on plane 1, along the vehicle central body wall, are shown in Fig. 17. Besides the comparison of the current laminar Navier–Stokes results and the experimental data, Fig. 17 also presents the pressure coefficient distribution obtained from the inviscid calculations for a similar grid. One can observe that, in the forward portion of the vehicle, the agreement between computational and experimental data is good.

There are discrepancies, however, in the boattail region. At the present time, the authors are not very concerned about these differences in the boattail region because previous experience with axisymmetric calculations[3] has indicated that a very fine mesh is

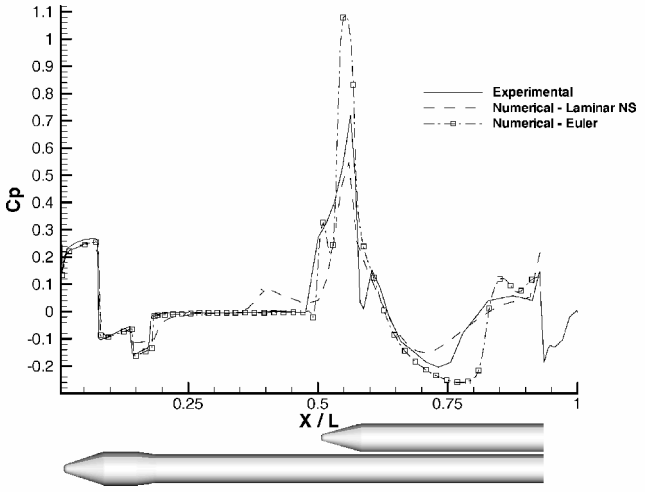

Fig. 17 Pressure coefficient distributions for plane 1 along central body wall for coarse grid laminar simulations ($M_\infty = 2$, $\alpha = 0$ deg, $Re = 1 \times 10^7$).

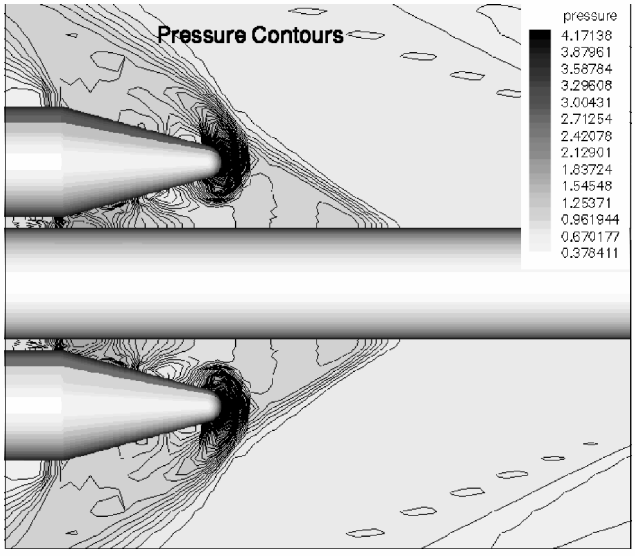

Fig. 18 Dimensionless pressure contours along plane 1 and over the surface of one booster for fine grid laminar simulations ($M_\infty = 2$, $\alpha = 0$ deg, $Re = 1 \times 10^7$).

required to correctly capture the flow topology in this region. Essentially, at supersonic freestream conditions, there is an oblique shock impinging on the boattail–afterbody cylinder intersection. This shock interacts with the body boundary layer, creating a region in which fairly complex flow phenomena are present and, hence, a very fine grid in the longitudinal direction is required for capturing the flow physics accurately. Such a fine grid in the boattail region was not used in the present case because the computational resources available would not allow for the needed refinement in this region, and there was an understanding that it would be more relevant, in the present case, to try to provide a better description of the region with strong interaction between the central body and boosters. Therefore, the discrepancies observed in the boattail region could be resolved by the use of meshes as fine, in this region, as the ones described in Ref. 3. Hence, it is a simple mesh refinement problem that can be fixed in the future after the other problems are sorted out.

A sudden increase in the pressure coefficient distribution is observed at $x/L \cong 0.35$ for the computational solution. The increase in C_p is due to the oblique shock wave created by the separation region along the central body. The experimental data do not indicate such a pressure coefficient increase, clearly indicating that the experimental measurements do not see an oblique shock wave in this region of the flow. The difference between experimental and numerical results could be explained by the flow being turbulent at $Re = 1 \times 10^7$. A turbulent boundary layer would not have separated as easily due to an adverse pressure gradient as did the laminar boundary layer. Hence, the flow separation upstream of the booster nose, which eventually is the originator of the oblique shock, can simply be a result of the treatment of the flow as laminar under conditions in which it is actually turbulent.

Farther downstream, at $x/L \cong 0.50$, the experimental measurements indicate a kink in the pressure coefficient distribution. This kink corresponds to the booster detached bow shock impingement on the central body. Clearly, the computational results do not display such an effect due to the presence of the oblique shock wave upstream of the boosters. The position of the pressure peak at $x/L \cong 0.57$ is correctly captured by the computation, although the magnitude of the pressure peak has a fairly significant error. There is a second pressure peak at $x/L \cong 0.61$, which the computational results simply ignore. Downstream of this second pressure peak, there is a region with reasonably good agreement between experimental and computational data, but, downstream of $x/L \cong 0.70$, the discrepancies between computational and experimental results again become significant. Note, however, that the computational mesh used in these simulations corresponds to the coarse grid.

A refined mesh was generated with $220 \times 50 \times 67$ grid points for the central body mesh and $200 \times 40 \times 33$ points for each of the booster meshes. As before, these numbers refer to grid points in the ξ, η, and ς directions, respectively. This grid is referred to here as the fine grid. Moreover, this grid only contains one-half of the central body and two boosters, yielding a total of approximately 1.3 million grid points, which was pretty much in the upper limit for the computational resources available to the authors at the time. This grid implies a factor of four increase in the azimuthal direction resolution of the central body grid and almost a factor of two increase in the longitudinal resolution of both the central body and booster grids. Furthermore, because these launchers fly only at very low angles of attack, the consideration that the flow is symmetric about the pitching plane is not a severe restriction in the usefulness of the computations for design work. The same flight condition was considered for the simulations with the fine grid. Therefore, $M_\infty = 2.0$, the angle of attack is zero, $Pr = 0.72$, and $Re = 1 \times 10^7$, based on the diameter of the central body of the vehicle.

Figure 18 presents pressure contours on plane 1 (Fig. 14) and along the surface of one of the boosters obtained with the fine grid. Figure 18 only shows the flowfield around the nose cap of the boosters. In this case, the oblique shock wave upstream of the boosters, due to the flow separation described earlier, is clearly evident in Fig. 18. Moreover, the detached shock in front of the boosters and its interaction with the oblique shock are also clearly seen in the pressure contours. The impingement of the detached shock, from the booster that is out of the plane with regard to this visualization, on the booster in the upper part of Fig. 18, is also seen along the conical section of the latter booster. Finally, the rapid flow expansion as it passes over the booster cone–cylinder intersection is also evident in Fig. 18. Hence, it is clear that the flow in this interaction region around the nose of the boosters is quite complex.

Pressure coefficient distributions along the central body, and on plane 1 (Fig. 14), are shown in Fig. 19. As before, Fig. 19 compares experimental and viscous computational results and it also includes the inviscid results for the same grid. It is clear that mesh refinement has improved the correlation between the results along the boattail region in the forward portion of the vehicle. However, the agreement is still not perfect in this region, but, as already discussed, the authors are not concerned about these discrepancies in the boattail region at the present time. The oblique shock wave due to flow separation ahead of the boosters is even more pronounced in this case, with a much better defined and stronger pressure jump at $x/L \cong 0.42$. The position of the pressure peak at $x/L \cong 0.57$ is again adequately captured by the calculation, but, as before, the magnitude of the peak is still smaller than the experimental value. The difference in C_p peak magnitude is, however, smaller in this case than it was for the coarse grid results. Moreover, as one can clearly see in Fig. 19, the

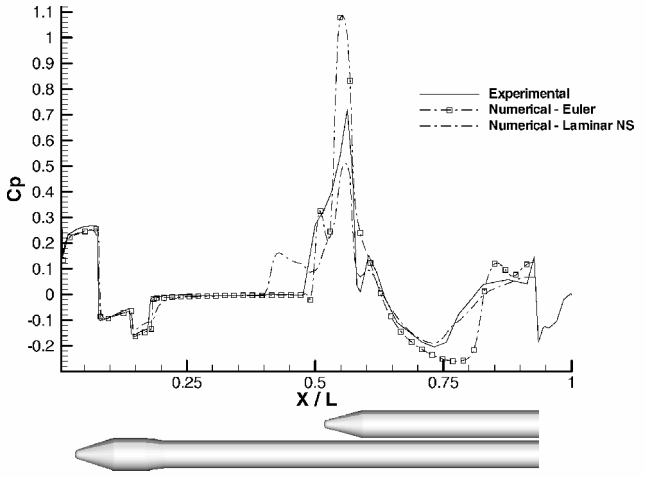

Fig. 19 Pressure coefficient distributions for plane 1 along central body wall for fine grid laminar simulations ($M_\infty = 2$, $\alpha = 0$ deg, $Re = 1 \times 10^7$).

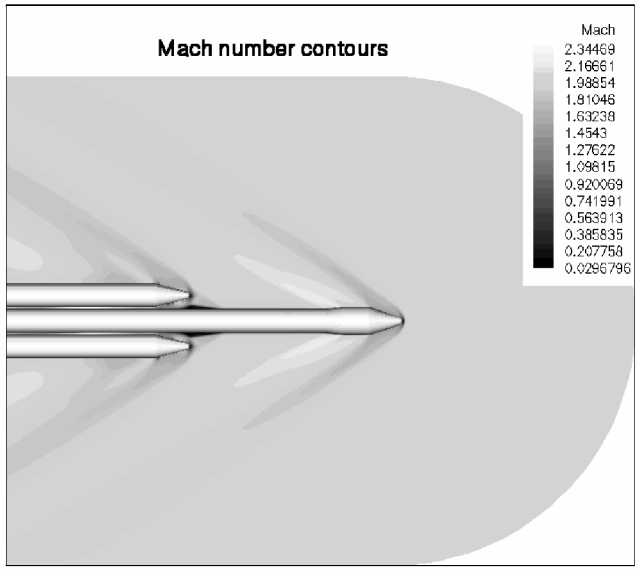

Fig. 20 Mach number contours in the field (plane 1) for turbulent simulations ($M_\infty = 2$, $\alpha = 0$ deg, $Re = 1 \times 10^7$).

simulation starts to capture the second pressure peak at $x/L \cong 0.61$. Furthermore, the agreement between experimental and computational C_p distributions downstream of this second pressure peak is remarkably good throughout the remainder of the vehicle. Note that the present computations do not represent the vehicle nozzle region, and, hence, it is not possible to match the results downstream of the $x/L \cong 0.92$ station. A comparison of the Euler calculations and the results in Fig. 19 indicate that the flow in the downstream sections of the vehicle include important viscous effects, and there would be no way to obtain good agreement between experiments and computation without the inclusion of the viscous terms in the formulation.

Turbulent Viscous Simulations

For the flight conditions considered here, which essentially involve VLS flows with Reynolds numbers on the order of 10^7, based on the body diameter, flowfields are clearly turbulent. Therefore, the implementation of turbulence models in the code is a necessary step to provide an adequate representation of the flows of interest. The long-term objective of this development work is to have a suite of models available in the code and let the user select the model that better suits the user's application. It is envisaged that, for the relevant flow conditions for the VLS, especially at angle of attack, a one-equation or a two-equation eddy viscosity model will be necessary for a correct representation of the flowfields. As an initial step toward this goal, a simple algebraic model has been implemented in the code so far. In particular, the algebraic Baldwin and Lomax[14] model is implemented in its standard form. This section describes some preliminary results obtained with this model.

The mesh used for the turbulent computations has $220 \times 50 \times 35$ points, in the ξ, η, and ς directions, respectively, for the central body grid and $180 \times 40 \times 33$ points for each booster grid. Note that this grid has the same number of points in the wall-normal direction as the fine grid used for the laminar calculations. To guarantee the adequate refinement near the wall, without increasing the computational cost, the stretching factor in the normal direction was slightly increased in comparison with the one used in the fine laminar grid. The important reduction in the number of grid points, with regard to the fine laminar grid, occurs in the circumferential direction for the central body grid. It was observed in the earlier computations that the refinement in this direction was not as critical to the accuracy of the solutions. As in the earlier case, the pitch plane is assumed to be a symmetry plane in the flowfield, and, hence, only one-half of the central body and two boosters are represented in the computational domain. The flight condition considered for these simulations is identical to the one considered in the earlier cases. Moreover, here the turbulent Prandtl number was set to 0.9, which is consistent with other results reported in the literature. Figure 20

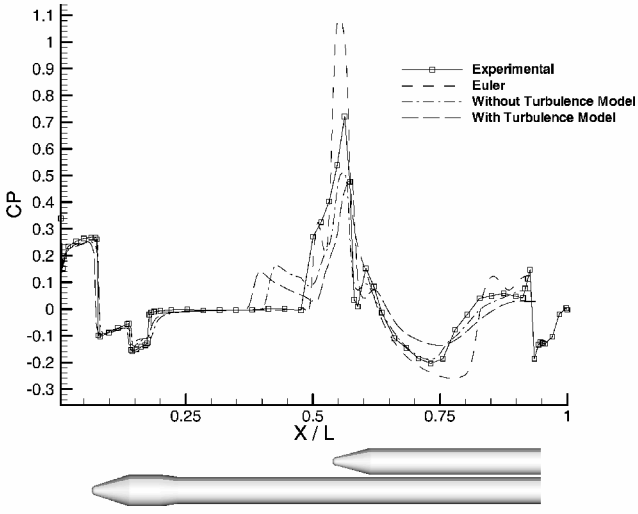

Fig. 21 Comparison of pressure coefficient distributions along the central body wall for plane 1 ($M_\infty = 2$, $\alpha = 0$ deg, $Re = 1 \times 10^7$).

presents the Mach number contours for this simulation in the plane containing the axes of the central body and two boosters (plane 1 in Fig. 14). An observation of Fig. 20 indicates that the flowfield solution in this case is not much different from that obtained for the laminar calculations with the fine grid. In particular, one can clearly see the flow separation ahead of the boosters and along the central body, as well as the oblique shock wave that is formed upstream of this separation region. Actually, the flow separation region seems to be even larger in this case, and it clearly extends farther upstream than in the laminar calculations.

Figure 21 presents a comparison of pressure coefficient distributions along the central body for plane 1 (Fig. 14). The curves shown in Fig. 21 include the experimental data, the turbulent computational results, and the laminar computational results obtained with the fine mesh. It is evident from Fig. 21 that the separation occurs farther upstream in the turbulent simulation when compared to the laminar solution. Such a result is contrary to what one would usually expect, that is, a smaller separation region in the turbulent case, and it is also in disagreement with the experimental data, which indicate no flow separation at this flight condition. The authors cannot offer a conclusive explanation for such behavior at this point, but they believe that the Baldwin–Lomax[14] model might be too overly simplified to be

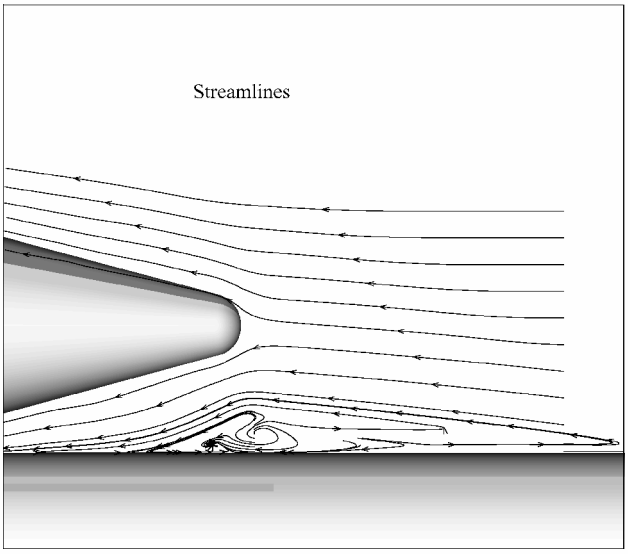

Fig. 22 Detail of streamlines around the separation region for turbulent simulations ($M_\infty = 2$, $\alpha = 0$ deg, $Re = 1 \times 10^7$).

able to capture the correct physics in the present flow situation. The authors have also started a research effort aimed at implementing more sophisticated turbulence models into the present code. This effort, however, is beyond the scope of the present paper.

Furthermore, the agreement between computation and experiment, in the region downstream of the second pressure peak ($x/L \cong 0.61$), is poorer for the turbulent simulations than it was for the laminar calculations on the fine grid. The two grids are not identical, but, based on the authors' experience with other launch vehicle simulations, the grids are sufficiently similar to rule out the possibility that the differences could only be credited to the grid. Furthermore, the fact that the turbulence model did not provide correct results upstream of the booster nose caps, as discussed earlier, raises the possibility that it could also be contributing to a poorer agreement at the present downstream location. It is also conceivable that, in such a region, where there is very close proximity between central body and booster, the flow is completely dominated by viscous effects. This would explain why a laminar solution yields better results than a turbulent one that implements a very simple turbulence model. Finally, Fig. 22 presents the flow streamlines in the region around the booster nose cap for the turbulent simulation, and it shows details of the separated flow in this region. It is clear that the computations are indicating a fairly complex separated region, certainly including secondary separation within the original reversed flow bubble. It is, actually, quite questionable whether the Baldwin and Lomax[14] model would truly be able to represent such a physically complex separated boundary layer if the computational results were an accurate representation of the experimentally observed flowfield. The experimental pressure distributions, however, show no evidence of a separation region in this portion of the vehicle at this flight condition.

The initial expectation was that the implementation of a turbulence model could help improve the correlation between numerical and experimental data, in comparison with the type of agreement obtained in the preceding section in which laminar computational results were reported. In particular, there was hope that the separation region upstream of the boosters would disappear and, hence, so would the oblique shock wave that is formed due to the separation. Clearly, this is not what the present results have shown. Furthermore, it is well known that the Baldwin and Lomax[14] model has a tendency to add more eddy viscosity than what would actually be the correct amount to represent the correct physical behavior of the boundary layer. Hence, this means that the model has a tendency of stabilizing boundary layers that, actually, should separate. This compounds even further the questions with regard to the present turbulent simulations. The authors believe that, at the present time, the best that can be said with regard to the turbulent simulations is that their validation is still an ongoing process. At the same time this paper was written, different meshes were being generated for this problem, and further analyses of the computational results were being performed. Fortunately, there are experimental results at different Reynolds numbers, for the same freestream Mach number, and these are being used to try to understand fully the discrepancies observed here. Furthermore, numerical parameters associated with the Baldwin and Lomax[14] model are also being parametrically evaluated to explain fully the model behavior in this case.

Conclusions

The paper describes inviscid and viscous computations over the complete VLS vehicle. These calculations use a chimera grid approach together with a finite difference numerical method to simulate supersonic flows over the complex VLS configuration, including the central body and the strap-on boosters. The present effort represents the first time that simulations over the complete VLS vehicle have been performed using such detailed structured grids. These simulations also represent the first time that numerical results obtained over the complete vehicle are detailed enough that one could seriously discuss their physical relevance and the flow topology in the region where there is close proximity between the central body and boosters. The capability to compute flowfields over such complex configurations was simply not available at IAE before the present effort.

Spatial discretization of the governing equations uses a central difference scheme, plus added artificial dissipation terms. These are formed as a blend of second and fourth differences, with an appropriate pressure switch that detects the present of strong pressure gradients. Temporal discretization uses an explicit, five-stage, second-order accurate Runge–Kutta time-stepping scheme with a spatially variable time-step option for convergence acceleration for steady-state problems. Algebraic grids are generated for each body of the complete configuration, and these are coupled together in a chimera sense to generate the complete composite grid for the overall configuration.

Despite that Reynolds numbers of interest are on the order of 10^7, laminar calculation results are presented for two different meshes for the sake of code development and validation. The first mesh for the viscous simulations has approximately 830,000 grid points, and it considers the complete vehicle. The other grid has approximately 1.3 million grid points and treats the pitch plane as a symmetry plane. Results for the fine grid calculations show very good qualitative agreement with the experimental data for pressure coefficient distributions, except for the appearance of an oblique shock upstream of the booster nose cap region due to flow separation of the central body boundary layer. In particular, the quantitative agreement of the pressure coefficient distributions, between experiments and fine grid computational results, is very good, and the differences are usually smaller than 5% throughout most of the vehicle. Clearly, there are some isolated points along the vehicle in which these differences can be much larger. The comparison also demonstrates the need to include the viscous terms to capture correctly the phenomena present in the region of strong aerodynamic interaction between central body and boosters. Finally, some preliminary results for turbulent simulations using the Baldwin and Lomax[14] algebraic eddy viscosity model are presented. Further analysis of these turbulent results is still necessary to establish their validity fully and to explain some of the discrepancies observed in comparison to the experimental data.

Acknowledgments

The present work was partially supported by the Conselho Nacional de Desenvolvimento Científico e Tecnológico (CNPq) under Integrated Project Research Grant 522.413/96-0. Additional support received from CNPq in terms of graduate scholarships for the first and second authors is also gratefully acknowledged. The authors are also indebted to Núcleo de Atendimento em Computação de Alto Desempenho and to Centro Nacional de Supercomputação, which have provided the computational resources used for the present simulations.

References

[1]Basso, E., Antunes, A. P., and Azevedo, J. L. F., "Three Dimensional Flow Simulations over a Complete Satellite Launcher with a Cluster Configuration," *Proceedings of the 18th AIAA Applied Aerodynamics Conference*, Vol. 2, AIAA, Reston, VA, 2000, pp. 805–813.

[2]Azevedo, J. L. F., Zdravistch, F., and Silva, A. F. C., "Implementation and Validation of Euler Solvers for Launch Vehicle Flows," *Proceedings of the Fourth International Symposium on Computational Fluid Dynamics*, Vol. 1, Univ. of California, Davis, CA, 1991, pp. 42–47.

[3]Azevedo, J. L. F., and Buonomo, C. A., "Axisymmetric Turbulent Simulations of Launch Vehicle Forebody Flows," AIAA Paper 99-3528, June–July 1999.

[4]Bigarelli, E. D. V., Mello, O. A. F., and Azevedo, J. L. F., "Three Dimensional Flow Simulations for Typical Launch Vehicle at Angle of Attack," *Proceedings of the 15th Brazilian Congress of Mechanical Engineering* [CD-ROM], Associação Brasileira de Ciências Mecânicas, Rio de Janeiro, 1999.

[5]Jameson, A., Schmidt, W., and Turkel, E., "Numerical Solutions of the Euler Equations by Finite Volume Methods Using Runge–Kutta Time-Stepping Schemes," AIAA Paper 81-1259, June 1981.

[6]Turkel, E., and Vatsa, V. N., "Effect of Artificial Viscosity on Three-Dimensional Flow Solutions," *AIAA Journal*, Vol. 32, No. 1, 1994, pp. 39–45.

[7]Yagua, L. C. Q., and Azevedo, J. L. F., "Application of the Chimera Technique for the Simulation of the 3-D Compressible Flow Equations," *Proceedings of the 15th Brazilian Congress of Mechanical Engineering* [CD-ROM], Associação Brasileira de Ciências Mecânicas, Rio de Janeiro, 1999.

[8]Wang, Z. J., and Yang, H. Q., "A Unified Conservative Zonal Interface Treatment for Arbitrarily Patched and Overlapped Grids," AIAA Paper 94-0320, Jan. 1994.

[9]Wang, Z. J., Buning, P., and Benek, J., "Critical Evaluation of Conservative and Non-conservative Interface Treatment for Chimera Grids," AIAA Paper 95-0077, Jan. 1995.

[10]Vieira, R., Azevedo, J. L. F., Fico, N. G. C. R., Jr., and Basso, E., "Three Dimensional Flow Simulation in the Test Section of a Slotted Transonic Wind Tunnel," *Proceeding of the 21st Congress of the International Council of the Aeronautical Sciences* [CD-ROM], International Council of the Aeronautical Sciences, Melbourne, Australia, 1998.

[11]Antunes, A. P., "Simulation of Aerodynamic Flows Using Overset Multiblock Meshes," M.S. Thesis, Dept. of Aeronautical Engineering, Instituto Tecnológico de Aeronáutica, São José dos Campos, Brazil, Aug. 2000 (in Portuguese).

[12]Pulliam, T. H., and Steger, J. L., "Implicit Finite Difference Simulations of Three-Dimensional Compressible Flow," *AIAA Journal*, Vol. 18, No. 2, 1980, pp. 159–167.

[13]Swanson, R. C., and Radespiel, R., "Cell-Centered and Cell-Vertex Multigrid Schemes for the Navier–Stokes Equations," *AIAA Journal*, Vol. 29, No. 5, 1991, pp. 697–703.

[14]Baldwin, B. S., and Lomax, H. L., "Thin Layer Approximation and Algebraic Model for Separated Turbulent Flows," AIAA Paper 78-257, Jan. 1978.

[15]Fletcher, C. A. J., *Computational Techniques for Fluid Dynamics*, 1st ed., Vol. 2, edited by J.-L. Armand, M. Holt, P. Hut, H.B. Keller, J. Killeen, S.A. Orszag, and V. V. Rusanov, Springer-Verlag, New York, 1988, pp. 101–121.

[16]Strauss, D., and Azevedo, J. L. F., "A Numerical Study of Turbulent Afterbody Flows Including a Propulsive Jet," *Proceedings of the 17th AIAA Applied Aerodynamics Conference*, AIAA, Reston, VA, 1999, pp. 654–664.

[17]Moraes, P., Jr., and Neto, A. A., "Aerodynamic Experimental Ivestigation of the Brazilian Satellite Launch Vehicle (VLS)," *Proceedings of the 3rd Brazilian Thermal Sciences Meeting*, Vol. 1, Associação Brasileira de Ciências Mecânicas, Rio de Janeiro, 1990, pp. 211–215.

R. M. Cummings
Associate Editor